Formation of CO2, H2 and condensed carbon from siderite dissolution in the 200–300°C range and at 50MPa

Vincent Milesi, François Guyot, Fabrice Brunet, Laurent Richard, Nadir Recham, Marc Benedetti, Julien Dairou, Alain Prinzhofer

FORMATION OF CO_2, H_2 AND CONDENSED CARBON FROM SIDERITE DISSOLUTION IN THE 200 – 300°C RANGE AND AT 50 MPa

Vincent Milesi[*] [a], François Guyot [b], Fabrice Brunet [c], Laurent Richard [d], Nadir Recham [e], Marc Benedetti [a], Julien Dairou [f] and Alain Prinzhofer [g]

[a] Équipe de Géochimie des Eaux,

Institut de Physique du Globe de Paris,

Sorbonne Paris Cité,

Université Paris Diderot,

UMR CNRS 7154,

F-75005 Paris, France.

[b] Institut de minéralogie et de physique des matériaux et de cosmochimie,

Sorbonne Université. Muséum National d'Histoire Naturelle,

UMR 7590, CNRS, UPMC, MNHN, IRD,

F-75005 Paris, France.

[c] ISTerre,

Université Joseph Fourrier,

UMR CNRS 5275,

38000 Grenoble, France.

[d] Geoquímics dels Àngels,

Carrer dels Àngels 4-2-1,

08001 Barcelona, Spain.

[e] Laboratoire de Réactivité et Chimie des Solides (LRCS)

Université de Picardie Jules Verne,

UMR CNRS 7314,

80039 Amiens, France.

[f] Univ Paris Diderot, Sorbonne Paris Cité,

Unité de Biologie Fonctionnelle et Adaptative (BFA),

UMR 8251 CNRS, Bioprofiler facility,

F-75205, Paris, France.

[g] IPEX&Co,

Rua Dezenove de Fevereiro 69/71, Botafogo, Rio de Janeiro,

22280-030 Rio de Janeiro, Bazil.

* Corresponding author:

E-mail address: milesi@ipgp.fr (Vincent Milesi)

Abstract

Laboratory experiments were conducted to investigate the chemical processes governing the carbon speciation associated to hydrothermal decomposition of siderite. Experiments were carried out in sealed gold capsules using synthetic siderite and deionised water. The samples were reacted at 200 and 300°C, under a pressure of 50 MPa. Siderite dissolved to reach the $3FeCO_3 + H_2O = Fe_3O_4 + 3CO_2 + H_2$ equilibrium and magnetite, Fe_3O_4, was produced accordingly. The gas phase was dominated by CO_2, H_2 and CH_4, the latter being in strong thermodynamic disequilibrium with CO_2. Contrary to the other gas products, H_2 concentration was found to decrease with run duration. TEM observations showed the occurrence of condensed carbon phases at the surfaces of magnetite and residual siderite grains. Thermodynamic calculations predict the formation of condensed carbon in the experiments according to the reaction: $CO_2 + 2H_2 \Rightarrow C + 2H_2O$, which accounted for the observed H_2 concentration decrease up to the point where H_2 and CO_2 activities were buffered by the graphite – siderite – magnetite assemblage. The well-organized structure of the carbon coating around magnetite emphasizes the high catalytic potential of magnetite surface for carbon reduction and polymerization. The formation of such C-rich phases may represent a potential source of CH_4 by hydrogenation. On the other hand, the catalysis of Fischer-Trospch type

61 reactions may be poisoned by the presence of carbon coating on mineral surfaces. In any case,
62 this study also demonstrates that abiotic H_2 generation by water reduction, widely studied in
63 recent years in ultrabasic contexts, can also occur in sedimentary contexts where siderite is
64 present. We show that, in the latter case, natural H_2 concentration will be buffered by a
65 condensed carbon phase associated with magnetite.

66

67 **1. INTRODUCTION**

68 Abiotic conversion of CO_2 into methane and more complex organic compounds is of
69 interest for a number of geochemical issues such as the global carbon cycle (e.g., Manning et
70 al., 2013) or the origin of life (e.g., Martin et al., 2008) and it has become a matter of interest
71 in the context of anthropogenic CO_2 sequestration (e.g., Petersen et al., 2005). In addition to
72 the thermal decomposition of organic matter, abiotic methane synthesis can be achieved
73 naturally by the hydrothermal alteration of ultrabasic rocks through serpentinization reactions
74 which generate highly reducing conditions (e.g., Neal and Stranger, 1983; Frost, 1985;
75 Abrajano et al., 1988; Kelley, 1996; Charlou et al., 1998; Kelley et al., 2001; Klein et al.,
76 2009; McCollom and Bach, 2009). Abiogenic methane associated with the serpentinization of
77 ultramafic rocks has been described in subaerial contexts (e.g., Abrajano et al., 1988; Lyon et
78 al., 1990; Fritz et al., 1992; Sano et al., 1993; Hosgormez et al., 2008; Etiope et al., 2011;
79 Suda et al., 2014) as well as in submarine environments from hydrothermal vents associated
80 with slow-spreading centers (e.g., Holm and Charlou, 2001; Kelley et al., 2001; Charlou et al.,
81 2002). Experimental studies suggested that under the hydrothermal conditions of
82 serpentinization reactions, abiotic generation of organic compounds can be attributed to a
83 Fischer-Tropsch-type (FTT) reaction (e.g., Berndt et al., 1996; Horita and Berndt, 1999;
84 McCollom and Seewald, 2001; Foustoukos and Seyfried, 2004; Fu et al., 2007), which

generally refers in the geological literature (and in the present study) to a surface-promoted reduction of an inorganic carbon source (frequently dissolved CO_2) to organic compounds.

Highly reducing hydrothermal conditions in a CO_2-bearing environment can also be achieved through the decomposition of siderite ($FeCO_3$) which is a ubiquitous carbonate component in sedimentary and metasedimentary rocks. Recently, Milesi et al. (2013) proposed that unconventional hydrocarbons could arise from siderite – water interactions in the source rock of the Solimões sedimentary basin in the North-West Brazil, which underwent high thermal stress due to magmatic intrusions (Mosmann et al., 1987; Rodrigues et al., 1990; Eiras and Lima, 2008). At higher temperatures, the decomposition of siderite has also often been invoked to explain the occurrence of reduced carbon in metamorphic rocks (e.g., Perry and Ahmad, 1977; Ueno et al., 2002). For example, van Zuilen et al. (2003) suggested that, in the carbonate-rich metasomatic rocks of the 3.8 Ga Isua Supracrustal Belt (Greenland), the presence of graphite was due to thermal decomposition of siderite at peak temperature conditions (between 500 and 600°C) according to the reaction:

$$\underset{\text{siderite}}{6\ FeCO_3} = \underset{\text{magnetite}}{2\ Fe_3O_4} + 5\ CO_2 + \underset{\text{graphite}}{C} \quad (1)$$

Zolotov and Shock (2000) and Steele et al. (2012) also proposed the decomposition of Fe-bearing carbonate as a source of reduced carbon in Martian meteorites. McCollom (2003) studied siderite decomposition in the presence of water vapor at 300°C. Magnetite was formed, along with CO_2 and H_2 as main gas products. Trace amounts of methane and light hydrocarbons were detected as well as alkylated aromatic compounds including polycyclic aromatic hydrocarbons (PAH).

In order to investigate the potential of siderite – water interactions to promote the formation of H_2-rich fluids and reduced carbon species, we carried out siderite dissolution

experiments at 200 - 300°C and 50 MPa. Dissolved organic compounds and gaseous species (H_2, CO_2, and CH_4) were analyzed on quenched samples. In addition, solid carbon products were looked for using transmission electron microscopy (TEM). Finally, the corresponding analytical results were discussed on the basis of a thermodynamic analysis.

2. MATERIALS AND METHODS

2.1 Starting materials

Siderite was synthesized in 25 mL stainless-steel Parr® autoclaves with a Teflon liner by dissolving 800 mg of iron sulfate heptahydrate ($FeSO_4 \cdot 7H_2O$) and 2 g of urea ($CO(NH_2)_2$) in 15 mL of oxygen-free deionized water. Oxygen-free water was prepared by bubbling argon into deionized water (Milli-Q) for one hour. In order to avoid iron oxidation, 40 mg of ascorbic acid were added to lower the pH down to a value of ~ 4, decreasing by 10^6 the kinetics of iron oxidation (e.g., Stumm and Lee, 1961; Singer and Stumm, 1970; Millero et al., 1987). The Parr bomb was then closed and heated at 180°C during 48 hours at the saturation vapor pressure of H_2O. The dissociation of iron sulfate and the total hydrolysis of urea resulted in high Fe^{2+} and dissolved inorganic carbon (DIC) concentrations. At 180°C, the NH_4^+/NH_3 couple released by the hydrolysis of urea imposed a basic pH of ca. 9.1 which promoted the precipitation of iron carbonate. The recovered material was rinsed three times in 50 mL of ethanol to eliminate water and potential organic contaminants generated from ascorbic acid. To eliminate traces of ethanol, the powder was dried by gradual heating from 25 to 70°C under primary vacuum during two hours. The synthesized material was then transferred into an argon box and stored into hermetic vials. The solid product was characterized as being single-phase siderite by X-ray powder diffraction (XRPD) (Fig. 1). Scanning electron microscopy (SEM) observations indicated typical grain sizes of tens of

micrometers (Fig. 1). This relatively large grain size prevented siderite from significant oxidation in air as indicated by the absence of iron oxide (XRPD and SEM) even in siderite products heated at 80°C in air for 12 hours (XRPD).

2.2 High-pressure and high-temperature experiments

The sample was contained in cylindrical gold capsules with a length of 20 mm and an outer diameter of 3.6 mm (wall thickness of 0.2 mm). Approximately 50 mg of siderite along with 100 µL of MilliQ water were loaded in the Au capsules, leaving a small headspace of air of less than 1/5 of the capsule volume. The capsule was welded shut and loaded in an externally heated cold-seal vessel (see Brunet and Chopin, 1995 for experimental details). Experiments were run from 3 hours to 4 months at 200 or 300°C under an argon pressure of 50 MPa. The uncertainty on the measured temperature is of +/- 1.5%. At the end of each experiment, power supply was switched off and the autoclave was quenched with an air stream. A single experiment was carried out at 300°C and 50 MPa using siderite in the absence of water (dry-siderite experiment).

2.3 Sampling and analysis methods

2.3.1 Gas products

The gaseous products trapped in the gold capsules at the end of the experiments were recovered and analyzed according to the procedure described in Malvoisin et al. (2013). This procedure consists in piercing the gold capsule in a plastic syringe containing a known volume of argon. A 250 µL aliquot of the gas mixture (gaseous products + Ar) was injected into a gas chromatograph coupled with a thermal conductivity detector (GC-TCD), allowing

155 the concentrations of H_2, CH_4 and CO_2 to be determined with detection limits of ~ 0.01, 0.05
156 and 0.5 *m*molal respectively (*m*molal equals *m*mol·kg^{-1} of solvent) . The GC column that we
157 used did not allow separating CO from air (N_2 and O_2) contamination. Therefore, only high
158 CO concentrations were detectable.

159 The gaseous products were recovered at ambient temperature and pressure. Under
160 these conditions, the Henry's Law constants (k_H) for H_2, CH_4 and CO_2, which are defined by

161 $$k_{Hi} = \frac{p_i}{c_i}$$

162 where p_i is the partial pressure of species *i* in the gas phase and c_i the concentration of species
163 *i* in the aqueous phase, have respective values of 127.4, 70.8 and 2.94 MPa·L·mol^{-1} as
164 calculated with the SUPCRT package (Helgeson et al., 1978; Johnson et al., 1992). Therefore
165 H_2, CH_4, and CO_2 will mostly concentrate in the gas phase and remaining dissolved H_2 and
166 CO_2 will be ignored in further mass balance calculation.

167

168 *2.3.2 Dissolved organic compounds*

169 In some experiments, a duplicate was carried out and devoted only to the analysis of
170 dissolved organic compounds. The aqueous solution was injected in a gas-chromatograph
171 coupled to a mass-spectrometer (GCMS). A GCMS-QP2010 Plus Shimadzu system with a
172 TRB-FFAP capillary columns (30 m × 0.25 mm ID × 0.5 μm; Teknokroma) was used. The
173 oven temperature was maintained at 40°C for 5 minutes and the heating program is as
174 follows: from 40 to 150°C at a rate of 10°C/min and maintain at 150°C for 5 minutes, then at
175 a rate of 40°C/min up to 275°C. The injection port temperature was 200°C, and helium was
176 used as the carrier gas at a pressure flow control mode of 110 kPa. A 1 μL sample aliquot was
177 injected in direct or split mode. The electron ionization energy was 70 eV, the ion source

temperature was 200°C, and the scan range was 30 – 150 m/z. The detection limits for carboxylic acids, alcohols and acetone are of ~ 0.2 *m*molal, ~ 0.01 *m*molal and ~ 0.01 *m*molal respectively. Due to evolution in time of the samples, only qualitative data of concentrations could be obtained for these dissolved organic compounds.

2.3.3 Solid products

The recovered powders were characterized by X-ray powder diffraction (XRPD) with a Bruker D5000 or D8 diffractometer using CuKα radiation. The instruments were operated with a step size of 0.026° 2θ and a counting time of 8 s. The divergence slit, anti-scatter slit, and detector slit were 0.6, 0.6, and 0.2 mm, respectively. The X-ray patterns were analyzed by Rietveld using the BGMN software (Taut et al., 1998). The recovered powders were observed by Scanning Electron microscopy (SEM), and Transmission Electron microscopy (TEM). SEM was performed on a Zeiss Ultra 55 FEG microscope operated at 10 kV and a working distance of 7.5 mm using mostly a detector of bacscattered electrons for imaging. This SEM is equipped with an energy dispersive X-ray system from Bruker. TEM was performed on a Jeol FEG 2100F operated at 200 kV equipped with an energy dispersive X-ray system from Jeol. Suspension in clean freshly opened absolute ethanol was prepared from the sample powders for TEM characterization. Vortex mixer and ultrasonic bath were used to disperse the powder homogenously within the ethanol medium. Five microliters of suspension were then deposited on a carbon filmed grid and left 10 minutes under confined atmosphere for ethanol evaporation.

2.4 Thermodynamic calculations

Reaction constants were calculated with the SUPCRT package (Johnson et al., 1992). The thermodynamic properties of siderite from Helgeson et al. (1978) were adjusted in order to better fit the experimental data. The $\Delta H°_f$ value adopted here for siderite was taken from Chai and Navrotsky (1994) of -750.6 (+/-1.1) $kJ \cdot mol^{-1}$, close to that of Helgeson et al. (1978) of -749.6 $kJ \cdot mol^{-1}$. The S° value of 105 $J \cdot mol^{-1} \cdot K^{-1}$ given by Helgeson et al. (1978) for siderite was reevaluated to 111.5 $J \cdot mol^{-1} \cdot K^{-1}$, which is a good compromise between the best experimental value of 109.5 (+/- 2) $J \cdot mol^{-1} \cdot K^{-1}$ determined by Bénézeth et al. (2009) and the best fit to the observed magnetite-siderite equilibrium (Figure 7).

No free gas phase was considered in the thermodynamic model. Indeed, calculations suggested that at the HP - HT experimental conditions of the experiments, gases from the headspace initially introduced in the gold capsule were entirely dissolved in the aqueous phase. Furthermore, at 300°C and 50 MPa, the saturation concentrations of H_2, CH_4, and CO_2 are of 1.67, 1.92, and 5.28 $mol \cdot L^{-1}$ respectively. These values are several orders of magnitude higher than those measured in the quenched samples (Table 1). Calculations showed that the same conclusion applies at 200°C. Thereby, H_2, CO_2 and CH_4 were consequently considered as aqueous species in further thermodynamic modeling.

3. RESULTS

We performed a series of eight HP - HT experiments at 50 MPa using siderite as starting material. Experimental conditions and gas analysis are listed in Table 1. Apart from the dry-siderite experiment, all samples reacted and yielded magnetite; however, residual siderite represented by far the most abundant phase in the recovered samples.

3.1 Gas products

All experiments performed in the siderite – water system yielded CO_2 as major component of the gas phase (Table 1). No gaseous product was detected in the dry-siderite experiment. In the 300°C runs, H_2 and CH_4 formed at concentrations two to three orders of magnitude lower than CO_2 concentrations. From sample *S300-1* to *S300-4*, the CO_2 and CH_4 concentrations increased while the maximal H_2 concentration observed was after 3 hours and then started decreasing (Fig. 2). In the longest experiments, i.e., *S300-3* to *S300-5*, the concentrations of CO_2, H_2 and the magnetite content remained constant suggesting attainment of a steady state. In contrast, the CH_4 concentration kept increasing but more slowly than in the first 168 hours. The slow accumulation of CH_4 throughout the run indicated a strong kinetic control over CH_4 formation (Table 1, Fig. 2).

In the 200°C experiments, CO_2 was the only detected gas; H_2 concentrations remained below the detection limit of the GC-TCD, i.e., <0.01 *m*molal. The experiments *S200-1* and *S200-2* yielded similar CO_2 concentrations around 4.5 *m*molal, i.e., approximately one order of magnitude lower than in the 300°C experiments (Table 1). In the two sets of experiments at 200 and 300°C, no significant CO signal was observed.

3.2 Dissolved organic compounds

To test potential contamination, the residual powder recovered from the dry-siderite experiment was rinsed with MilliQ water which was further analyzed. Formic-acid (HCOOH), acetic-acid (CH_3COOH), methanol (CH_3OH), ethanol (C_2H_5OH), propanol (C_3H_7OH) and acetone (C_3H_6O) were detected. Formic acid, acetic acid and ethanol were the main species observed in the 0.1 – 1 *m*molal range, while methanol, propanol and acetone were detected at concentrations one order of magnitude below. Similar ranges of

concentration were measured in the hydrothermal experiments on siderite at 200 and 300°C. In the following mass balance calculations, the concentrations of these dissolved organic compounds, which are more than one to two orders of magnitude lower than CO_2 concentrations, will be neglected.

3.3 Solid products

XRPD patterns are dominated by siderite along with minor magnetite (Fig. 3). Quantitative XRPD analysis allowed estimation of the Fe_3O_4 content to less than 5 wt.% (+/- 1%) of the powder in all experiments. The XRPD pattern of the residual powder from *S300-1* showed that at 300°C, Fe_3O_4 had already formed after three hours. In the experiments performed at 200°C, the magnetite content was constant with values of ~ 3 wt.% (+/-1%) of the powder.

On SEM images in backscattered electron mode, iron oxide shows typical grain sizes of ~ 100 nm but grains of magnetite larger than 1 µm were also observed (Fig. 3a). The presence of etch pits on the siderite surface indicates partial dissolution and confirms thereby the residual character of siderite. Furthermore, magnetite grains are partly embedded in the siderite surface emphasizing the genetic link between Fe_3O_4 and the iron carbonate (Fig. 3b).

TEM analyses of the solid products of the two sets of experiments at 200 and 300°C showed the presence of a condensed phase, rich in carbon (Fig. 4). Such a phase was carefully looked for in the starting materials but was never observed. This phase appeared to be highly unstable under the electron beam and could therefore be hydrated or hydrogenated. It showed no obvious spatial relationship with siderite or magnetite.

In the 200°C experiments, another carbon-rich phase was observed as regular nm-sized coats around magnetite and siderite grains (Fig. 5). The carbon matter which encapsulates magnetite grains is made of a stack of layers, presumably short graphene units, suggesting a relatively well organized state (Fig. 5a). When associated to siderite, the carbon coats are less continuous and displayed a lower organization level (Fig. 5b). In both *S200-1* and *S200-2*, the carbon coat is ~ 5 nm thick. In the 300°C experiments, well defined carbon layers are not observed. At the surface of magnetite grains, they are present on some faces and are less than 1 nm thick. They would deserve further studies. At the surface of siderite, larger reaction zones are made of a complex phase assemblage. Electron diffraction patterns and EDXS analyses suggest that they are constituted of iron oxide (either FeO or Fe_3O_4) closely associated to a solid carbon-rich phase (Fig. 6).

4. THERMODYNAMIC MODEL

4.1 Mass balance

Thermal decomposition of siderite upon heating occurs between ~ 400 and 600°C depending on pressure, heating rate, CO_2 and O_2 fugacities (e.g. French and Rosenberg, 1965; Gallagher and Warne, 1981; Dhupe and Gokarn, 1990; Jagtap et al., 1992; Pillot et al., 2013). The dry-siderite experiment performed at 300°C and 50 MPa yielded no detectable gaseous phases nor secondary solid products, indicating that thermal decomposition of siderite was not substantial and yielded fugacities of CO_2 which were not detected. In experiments with water at 300°C (50 MPa), the production of magnetite, CO_2 and H_2 is thus consistent with decomposition of siderite due to a dissolution process:

$$3\ FeCO_3 + H_2O_{,aq} = Fe_3O_4 + 3\ CO_{2,aq} + H_{2,aq} \quad (2)$$

At 200°C and 50 MPa whatever the run duration, CO_2 and magnetite formed but no H_2 was detected. Calculations with SUPCRT under these temperature and pressure conditions indicated that magnetite is stable for a H_2 concentration above 10^{-3} *m*molal. Such H_2 concentration threshold is below detection limit of our GC but yet corresponds to significant yields of H_2, suggesting that Reaction (2) also occurred at 200°C.

In all experiments, no significant CO signal was observed; Seewald et al. (2006) showed that in reducing hydrothermal conditions, CO equilibrates rapidly with CO_2 thanks to kinetically fast water-gas shift reaction

$$CO_{2,aq} + H_{2,aq} = CO_{,aq} + H_2O_{(l)} \quad (3)$$

According to Reaction (3), CO concentrations at 200 and 300°C must have reached 10^{-7} and 10^{-2} *m*molal respectively, which is negligible in comparison to the amount of produced CO_2.

In experiments of siderite decomposition in the presence of water vapor at 300°C, McCollom (2003) found a CO_2/H_2 ratio of 2.5 consistent with Reaction (2). In our experiments, considering Reaction (2), it is possible to calculate the H_2 concentration corresponding to the amount of measured CO_2 and to compare it with the measured H_2 (Table 2). Organic molecules detected by GCMS were neglected in the carbon and hydrogen mass balance due to their low concentration in comparison to that of CO_2. From experiments *S300-1* to *S300-5*, the amount of missing H_2 increases from ~ 20 to 150 *m*molal. The amounts of O_2 and N_2 introduced initially in the Au capsule through the headspace of air were estimated to 10 and 40 *m*molal, respectively. Part of the missing H_2 can potentially be accounted for by the reaction of O_2 and N_2 with H_2 to form H_2O and NH_3, respectively according to the following reactions:

$$2\ H_{2,aq} + O_{2,aq} = 2\ H_2O_{,aq} \quad (4)$$

316 $$N_{2,aq} + 3\ H_{2,aq} = 2\ NH_{3,aq} \quad (5)$$

317 Considering an H_2 concentration at equilibrium with the siderite – magnetite – graphite
318 mineral assemblage, ~ 20 and 4 *m*molal of H_2 would be consumed through reactions (4) and
319 (5), respectively. The amount of missing H_2 in experiment *S300-1* is consistent with a total
320 reduction of O_2 (Table 2); however, after complete O_2 consumption, H_2 concentration should
321 increase with the advancement of Reaction (2). In contrast, the H_2 concentration decreased
322 from 12.1 to 1.5 *m*molal between samples *S300-1* and *S300-5*. Neither the reduction of O_2
323 (Reaction 4) nor the production of ammonia (Reaction 5) can account for the ~ 150 *m*molal of
324 missing H_2 in experiment *S300-5*. The dissolved organic compounds detected in the *m*molal
325 range cannot either explain the lack of H_2. The formation of condensed carbon that is
326 observed at 200 and 300°C (Fig. 4 and 5) is another way to consume H_2 according to the
327 reaction:

328 $$CO_{2,aq} + 2\ H_{2,aq} = C_{(\text{“graphite”})} + 2\ H_2O \quad (6)$$

329 Considering Reaction (6), ~ 60 *m*mol of condensed carbon per kg of solution could have
330 formed. That is, 1.6% of the carbon initially introduced as siderite would have been converted
331 into a carbonaceous phase, which would then be the dominant species produced by CO_2
332 reduction in our experiments. Considering a typical grain size of the starting siderite material
333 of 20 µm (Fig. 1), calculations show that such an amount would be equivalent to a carbon
334 layer of 20 nm in thickness at the surface of siderite grains, which is qualitatively consistent
335 with the TEM observations (Fig. 6). We note that the organic contamination in the starting
336 material would not contribute significantly to solid-state organic carbon even though it would
337 be totally converted into this phase.

338

339 **4.2 Thermodynamic calculations**

Data obtained at 300°C were plotted along with the calculated stability domains of hematite, magnetite, wüstite and siderite as well as the CO_2 – graphite equilibrium in a $\log m_{H_{2(aq)}}$ - $\log m_{CO_{2(aq)}}$ diagram (Fig. 7). Mineral stability domains were calculated at 300°C (+/- 1.5%). The best consistency between calculation and measured data is achieved at a temperature of 295 °C which is within the experimental error bar. All the data points plot close to the siderite-magnetite equilibrium (Fig. 7), including *S300-1* (3 hours). At the timescale of the experiments, the relatively fast kinetics of Reaction (2) should impose a constant aH_2/aCO_2 ratio. However, the constant evolution towards lower H_2 and higher CO_2 concentrations indicates that a slower reaction operated concurrently. In experiments *S300-3* to *S300-5* which lasted 144 and 2880 hours, respectively, the CO_2 - H_2 concentrations plot near the magnetite – siderite – graphite equilibrium point. This suggests that the evolution of CO_2 and H_2 activities towards this point results from the production of a carbon-rich phase, arising from the reduction of CO_2 according to Reaction (6). This is consistent with the TEM observations of condensed carbon products (Fig. 4, 5 and 6). After ~ 150 hours (i.e., experiments *S300-3* to *S300-5*), the magnetite – siderite – "graphite" mineral assemblage buffers the CO_2-H_2 concentrations (Fig. 2 and 7). Neglecting further hydrocarbons production, an equilibrium for siderite dissolution might thus have been reached. Alternatively, the dissolution of siderite could have stopped for kinetic reasons due to secondary phases deposited at its surface. The detailed composition of the aqueous phase would be required to investigate this issue.

5. DISCUSSION

5.1 Occurrence of condensed carbonaceous matter

Different forms of condensed carbonaceous material were observed under the TEM in samples reacted at 200 and 300°C. At 200°C, condensed carbon is located at magnetite and siderite grain surfaces and occurs in the form of a few stacks of graphene layers (ca. 5 nm), especially when encapsulating magnetite (Fig. 5a). At 300°C, condensed carbon was found intimately associated with aggregates of iron oxide of yet undetermined form (either FeO or Fe_3O_4) covering siderite crystals (Fig. 6). In addition, in the two sets of experiments (200 and 300°C), an electron-beam sensitive carbonaceous compound was observed which is interpreted as hydrated or hydrogenated carbon, possibly a PAH (Fig. 4). The occurrence of condensed carbonaceous material in relatively large amount, indicates that part of the CO_2 initially contained in siderite, has been reduced. The CO_2 reduction in the presence of H_2 to form condensed carbon, assumed to be graphite for the sake of the calculation, is consistent with thermodynamic predictions. In turn, the proximity of experimental data points to the CO_2 - graphite equilibrium suggests that the thermodynamic properties of the observed carbonaceous phases are in first approximation well described by those of graphite.

The possibility of carbonaceous matter formation in the C-O-H system at high pressure and high temperature has already been mentioned in several experimental studies. In serpentinization experiments at 300°C and 50 MPa, Berndt et al. (1996) reported a large deficit in the CO_2 mass balance that they explained by the likely precipitation of graphite or amorphous carbon. In experiments with CO_2 - H_2 rich fluids and Fe - Ni catalysts at 50 MPa in the 200 – 400°C temperature range, Horita and Berndt (1999) showed that combined concentrations of ΣCO_2 (total dissolved carbonate species) and CH_4 in the fluid decreased in the early stages of the experiments until it finally rebounded. It was suggested that the transient formation of formate ion ($HCOO^-$), carbon monoxide or condensed carbon phases could have acted as a carbon sink. It can be shown that CO_2 and H_2 concentrations reported in

387 the studies by Berndt et al. (1996) and Horita and Berndt (1999) clearly plot inside the
388 graphite stability field, which supports the assumption of carbonaceous matter precipitation.

389 Dufaud et al. (2009) carried out experiments of Mg-rich silicate carbonation at 400 -
390 500°C and 100 MPa. The authors mentioned the formation of an ill-ordered graphitic phase,
391 accounting for up to 22% of the total carbon budget. In experiments with C-H-O fluids under
392 graphite undersaturation, at 600°C and 1 GPa, Foustoukos (2012) reported the formation of
393 poorly ordered graphitic carbon that may account for up to 60% of the total carbon of the
394 system. In low-temperature (55 – 100°C) water-rock experiments with ultramafic and mafic
395 rocks and minerals, Mayhew et al. (2013) showed H_2 production within the first few hours,
396 followed by a slow decrease with time, as we observed in the present study. Interestingly, in a
397 $\log m_{H_{2(aq)}}$ - $\log m_{CO_{2(aq)}}$ diagram, their final CO_2 - H_2 concentrations plot right on the
398 equilibrium point between magnetite, siderite and graphite; however neither iron carbonate
399 nor condensed carbon was detected.

400 Precipitation of carbonaceous phases has been frequently described in experimental
401 studies of Fischer-Tropsch synthesis for industrial purposes. For example, in experiments at
402 300°C, 1.5 MPa and a H_2/CO ratio of 1, Galuszka et al. (1992) identified with FTIR
403 spectroscopy and thermogravimetry five forms of carbonaceous material (aliphatic, aromatic,
404 oxygenated, carbidic and amorphous) deposited on the iron catalysts. In experiments of
405 Fischer-Tropsch synthesis at 270°C by Sarkar et al. (2007), reactions between CO and H_2 to
406 form alkanes produced collateral H_2O, which oxidized the carbide-iron catalyst (Fe_5C_2) into
407 magnetite. The authors detected ordered and amorphous carbon coatings (ca. 5 nm thick)
408 encapsulating newly formed magnetite. They attributed the formation of these carbon layers
409 to Boudouard reactions such as:

410 $$2\ CO = CO_2 + C \qquad (7)$$

411 Although no CO intermediates could be detected in the present experiments, it cannot be
412 excluded that a similar reaction process led to the formation of the carbon coatings observed
413 around both magnetite and siderite grains in the present study (Fig. 5).

414

415 **5.2 Implication for mineral surface catalysis of CO_2 reduction**

416 The production of complex carbon compounds, such as PAH, in experiments of
417 hydrothermal decomposition of siderite with water vapor, was interpreted by McCollom
418 (2003) as related to surface catalyzed processes. Magnetite was proposed by Voglesonger
419 (2001) to enhance the production of methanol from CO_2 - H_2 rich fluids in hydrothermal
420 conditions. In experiments with CO_2 - H_2 rich fluids and magnetite at 400°C and 50 MPa, Fu
421 et al. (2007) measured, using combustion, significant amounts of carbon-bearing compounds
422 located at the magnetite surface. Magnetite is often invoked as a potential mineral catalyst in
423 experiments involving FTT reactions (Horita and Berndt, 1999; McCollom and Seewald,
424 2001; Foustoukos and Seyfried, 2004); however, McCollom (2013) pointed out that none of
425 the latter studies provides definitive evidence that magnetite can catalyze carbon reduction in
426 hydrothermal environments. Recently, Mayhew et al. (2013) showed from water-rock
427 interaction experiments performed at low-temperature (55 – 100°C), that the spinel structure
428 of Fe-bearing minerals such as magnetite is highly beneficial for electron transfer processes.
429 In our experiments, observations of condensed carbon encapsulating magnetite and siderite
430 highlight the catalytic role of mineral surfaces in the processes of carbon reduction and
431 polymerization (Fig. 5). The relatively high organization degree of the carbon surrounding
432 magnetite points to a higher catalytic ability for this latter mineral.

433 In addition to the condensed carbonaceous material, the experiments yielded an
434 electron-beam sensitive carbonaceous compound, interpreted as hydrated or hydrogenated

carbon, possibly a PAH (Fig. 4). McCollom et al. (1999) and McCollom and Seewald (2003) carried out experiments with aqueous solution of formic acid at temperature higher than 175°C. McCollom and Seewald (2003) observed that only the experiments containing a gaseous phase, i.e., that of McCollom et al. (1999), yielded complex hydrocarbons. They suggested that the presence of liquid water may interfere with the formation of C-C bonds on the catalyst surface. As our experiments operated without a gaseous phase, a measurable yield of hydrated or hydrogenated chains of carbon suggests that presence of liquid water does not entirely preclude the polymerization of carbon.

In the 300°C experiments especially, graphitic carbon was also observed closely associated to aggregates of magnetite or FeO at the siderite surface (Fig. 6). The reduction of CO_2 released by the carbonate may have been catalyzed by the iron oxide present on the siderite surface, resulting in a local and rapid precipitation of graphitic carbon. A similar process was proposed by Sarkar et al. (2007) with reaction between carbide iron (Fe_5C_2) and water producing closely associated magnetite and elemental carbon.

5.3 H_2 and CH_4 generation

A main implication of our study to natural systems is that abiotic H_2 generation, widely studied in recent years in ultrabasic contexts, could also occur in sedimentary basin in conjunction with hydrothermal dissolution of siderite. According to our experiments, H_2 concentrations of ~ 1 *m*molal at 300°C are to be expected in the presence of graphitic carbon, a potential by-product of siderite dissolution. Such concentrations are comparable to those reported by Charlou et al. (2001) at the Rainbow hydrothermal field (i.e., 1 – 10 *m*molal). Moreover, TEM observations coupled to thermodynamic modeling showed that siderite – water interactions drove the H_2-CO_2 activity to values which allowed the production of

condensed carbon from CO_2. However, it remains unclear whether the CH_4 produced in our experiments is also related to siderite dissolution. Abiotic generation of CH_4 is frequently attributed to the reduction of CO_2 according to the reaction

$$CO_2 + 4\ H_2 = CH_4 + 2\ H_2O \quad (8)$$

(e.g., Berndt et al., 1996; Horita and Berndt, 1999; McCollom and Seewald, 2001; Foustoukos and Seyfried, 2004; Fu et al., 2007). However, experiments carried out with C-O-H fluids under hydrothermal conditions with isotope labeling of the carbon source showed that most of the measured CH_4 often results from a background source (McCollom and Seewald, 2001; 2003a; Seewald, 2006). Detection of carboxylic acids and ethanol in the dry-siderite experiment indicates that traces of organic compounds were already present in the starting material. A contribution of this organic contamination to methane production cannot be excluded and therefore it is not possible to conclude on the origin of the measured CH_4.

Considering Reaction (8), the thermodynamic calculation predicts a CO_2/CH_4 ratio in our experiments of ~ 1; however, we observed in *S300-5* a ratio of ~ 1000, close to the one reported by McCollom (2003) in experiments of hydrothermal decomposition of siderite with water vapor. This result emphasizes the strong kinetics limitation on CH_4 formation through CO_2 reduction by H_2-rich aqueous fluids in the 200 – 300°C range. For example, based on experiments performed with C-O-H fluids and no mineral phases, Seewald et al. (2006) proposed that kinetic limitations may preclude the reduction of methanol into methane in the cascade of reduction from CO_2 to CH_4. As a consequence, in serpentinization experiments, the generation of CH_4 through CO_2 reduction is frequently assumed to be a surface catalyzed process (Berndt et al., 1996; Horita and Berndt, 1999; McCollom and Seewald, 2001; Foustoukos and Seyfried, 2004; Fu et al., 2007). In that respect, coating of mineral surfaces by carbon as observed here, is expected to poison the surface catalysis of CO_2 reduction. On

the other hand, the presence of condensed carbon shows that CO_2 reduction can operate at low temperature (200 - 300°C) at least in the presence of mineral surfaces (magnetite and to a smaller extend siderite). Then, the presence of carbonaceous material offers new pathways to the formation of CH_4 through hydrogenation reactions

$$C + 2\ H_2 = CH_4 \quad (9)$$

However, considering Reaction (9), the CH_4 concentrations in our experiments remained far from equilibrium with the carbonaceous material, which suggests that this alternative route to produce CH_4 is also kinetically unfavourable. Parameters affecting the thermodynamics or the kinetics of Reaction (9), such as total pressure, catalysts or the exact structure of the carbonaceous phase need to be further investigated.

ACKNOWLEDGEMENTS

This work was supported by the HRT Oil&Gas and IPEX&Co company. The authors are grateful for the constructive comments of Tom McCollom, Dionysis Foustoukos and an anonymous reviewer. We appreciate stimulant discussion and technical supports from Benjamin Malvoisin, Olivier Sissmann, Nathaniel Findling and Martine Lanson. We are also thankful to René Rodriguez and all members of the department of stratigraphy and paleontology of the University of State of Rio de Janeiro.

REFERENCES

Abrajano T. A., Sturchio N. C., Bohlke J. K., Lyon G. L., Poreda R. J. and Stevens C. M. (1988) Methane-hydrogen gas seeps, Zambales Ophiolite, Philippines: Deep or shallow origin? *Chem. Geol.* **71**(1), 211-222.

506 Bénézeth P., Dandurand J. L. and Harrichoury J. C. (2009) Solubility product of siderite
507 ($FeCO_3$) as a function of temperature (25-250 °C). *Chem. Geol.* **265**(1-2), 3-12.

508 Berndt M. E., Allen D. E. and Seyfried Jr., W. E. (1996) Reduction of CO_2 during
509 serpentinization of olivine at 300°C and 500 bar. *Geology* **24**(4), 351-354.

510 Berndt M. E., Allen D. E. and Seyfried Jr., W. E. (1996) CORRECTION. *Geology* **24**(7), 671.

511 Brunet F. and Chopin C. (1995) Bearthite, $Ca_2Al(Po_4)_2OH$: Stability, thermodynamic
512 properties and phase-relations. *Contrib. Mineral. Petr.* **121**(3), 258-266.

513 Chai L. and Navrotsky A. (1994) Enthalpy of formation of siderite and its application in
514 phase equilibrium calculation. *Am. Mineral.* **79**(9-10), 921-929.

515 Charlou J. L., Fouquet Y., Bougault H., Donval J. P., Etoubleau J., Jean-Baptiste P., ... and
516 Rona P. A. (1998) Intense CH_4 plumes generated by serpentinization of ultramafic rocks at
517 the intersection of the 15° 20′ N fracture zone and the Mid-Atlantic Ridge. *Geochim.*
518 *Cosmochim. Ac.* **62**(13), 2323-2333.

519 Charlou J. L., Donval J. P., Fouquet Y., Jean-Baptiste P. and Holm N. (2002) Geochemistry
520 of high H_2 and CH_4 vent fluids issuing from ultramafic rocks at the Rainbow hydrothermal
521 field (36°14′N, MAR). *Chem. Geol.* **191**(4), 345-359.

522 Dufaud F., Martinez I. and Shilobreeva S. (2009) Experimental study of Mg-rich silicates
523 carbonation at 400 and 500°C and 1 kbar. *Chem. Geol.* **265**(1-2), 79-87.

524 Dhupe A. P. and Gokarn A. N. (1990) Studies in the thermal decomposition of natural
525 siderites in the presence of air. *Int. J. Miner. Process.* **28(**3–4), 209-220.

526 Eiras J. F. and Lima C. C. A. (2008) Petroleum exploration in the Solimões basin. *PetroGeo*.

527 Etiope G., Schoell M. and Hosgörmez H. (2011) Abiotic methane flux from the Chimaera
528 seep and Tekirova ophiolites (Turkey): understanding gas exhalation from low temperature
529 serpentinization and implications for Mars. *Earth Planet. Sc. Lett.* **310**(1), 96-104.

530 Foustoukos D. I. and Seyfried Jr., W. E. (2004) Hydrocarbons in hydrothermal vent fluids:
531 The role of chromium-bearing catalysts. *Science* **304**(5673), 1002-1005.

532 Foustoukos D. I. (2012) Metastable equilibrium in the C-H-O system: Graphite deposition in
533 crustal fluids. *Am. Mineral.* **97**(8-9), 1373-1380.

534 French B. M. and Rosenberg P. E. (1965) Siderite $FeCO_3$: thermal decomposition in
535 equilibrium with graphite. *Science*, **147**, 1283-1284.

536 Fritz P., Clark I. D., Fontes J. C., Whiticar M. J. and Faber E. (1992) Deuterium and ^{13}C
537 evidence for low temperature production of hydrogen and methane in a highly alkaline
538 groundwater environment in Oman. *Water-Rock Interaction*, 793-796.

539 Frost B. R. (1985) On the stability of sulfides, oxides, and native metals in serpentinite. *J.*
540 *Petrol.* **26**(1), 31-63

541 Fu Q., Sherwood Lollar B., Horita J., Lacrampe-Couloume G. and Seyfried Jr., W. E. (2007)
542 Abiotic formation of hydrocarbons under hydrothermal conditions: Constraints from chemical
543 and isotope data. *Geochim. Cosmochim. Ac.* **71**(8), 1982-1998.

544 Gallagher P. K. and Warne S. St. J. (1981) Thermomagnetometry and thermal decomposition
545 of siderite. *Thermochim. Acta* **43**(3), 253-267.

546 Galuszka J., Sano T. and Sawicki J. A. (1992) Study of carbonaceous deposits on Fischer-
547 Tropsch oxide-supported iron catalysts. *J. Catal.* **136**(1), 96-109.

548 Helgeson H. C., Delany J. M., Nesbitt H. W. and Bird D. K. (1978) Summary and critique of
549 the thermodynamic properties of rock-forming minerals. *Am. J. Sci.* **278A**, 1-229.

550 Holm N. G. and Charlou J. L. (2001) Initial indications of abiotic formation of hydrocarbons
551 in the Rainbow ultramafic hydrothermal system, Mid-Atlantic Ridge. *Earth Planet. Sc. Lett.*
552 **191**(1-2), 1-8.

553 Horita J. and Berndt M. E. (1999) Abiogenic methane formation and isotopic fractionation
554 under hydrothermal conditions. *Science* **285**(5430), 1055-1057.

555 Hosgormez H., Etiope G. and Yalcin M. N. (2008) New evidence for a mixed inorganic and
556 organic origin of the Olympic Chimaera fire (Turkey): a large onshore seepage of abiogenic
557 gas. *Geofluids* **8**(4), 263-273.

558 Jagtap S. B., Pande A. R. and Gokarn A. N. (1992) Kinetics of thermal decomposition of
559 siderite: effect of particle size. *Int. J. Miner. Process.* **36**(1–2), 113-124.

560 Johnson J. W., Oelkers E. H. and Helgeson H. C. (1992) SUPCRT92: A software package for
561 calculating the standard molal thermodynamic properties of minerals, gases, aqueous species,
562 and reactions from 1 to 5000 bar and 0 to 1000°C. *Comput. Geosci.* **18**(7), 899-947.

563 Kelley D. S. (1996) Methane-rich fluids in the oceanic crust. *J. Geophys. Res. – Sol. Ea.*
564 **101**(B2), 2943-2962.

565 Kelley D. S., Karson J. A., Blackman D. K., Früh-Green G. L., Butterfield D. A., Lilley M.
566 D., ... and Rivizzigno P. (2001) An off-axis hydrothermal vent field near the Mid-Atlantic
567 Ridge at 30 N. *Nature* **412**(6843), 145-149.

568 Klein F., Bach W., Jöns N., McCollom T. M., Moskowitz B. and Berquó T. (2009) Iron
569 partitioning and hydrogen generation during serpentinization of abyssal peridotites from 15°N
570 on the Mid-Atlantic Ridge. *Geochim. Cosmochim. Ac.* **73**(22), 6868-6893.

571 Lyon G. L., Giggenbach W. F. and Lupton J. F. (1990) Composition and origin of the
572 hydrogen-rich gas seep, Fiordland, New Zealand. *Eos* **71**, 1717.

573 Malvoisin B., Brunet F., Carlut J., Montes-Hernandez G., Findling N., Lanson M., Vidal O.,
574 Bottero J. Y. and Goffé B. (2013) High-purity hydrogen gas from the reaction between BOF
575 steel slag and water in the 473–673 K range. *Int. J. Hydrogen Energ.* **38**(18), 7382-7393.

576 Manning C. E., Shock E. L. and Sverjensky D. A. (2013) The chemistry of carbon in aqueous
577 fluids at crustal and upper-mantle conditions: Experimental and theoretical constraints. In:
578 *Carbon in Earth* (eds. R.M. Hazen, A.P. Jones, J.A. Baross), *Rev. Mineral. Geochem.* **75**, pp.
579 109-148. Mineralogical Society of America.

580 Martin W., Baross J., Kelley D. and Russell M. J. (2008) Hydrothermal vents and the origin
581 of life. *Nat. Rev. Microbiol.* **6**(11), 805-814.

582 Mayhew L. E., Ellison E. T., McCollom T. M., Trainor T. P. and Templeton A. S. (2013)
583 Hydrogen generation from low-temperature water-rock reactions. *Nat. Geosci.* **6**, 478-484.

584 McCollom T. M., Ritter G. and Simoneit B. R. (1999) Lipid synthesis under hydrothermal
585 conditions by Fischer-Tropsch-type reactions. *Origins Life Evol. B.* **29**(2), 153-166.

586 McCollom T. M. and Seewald J. S. (2001) A reassessment of the potential for reduction of
587 dissolved CO_2 to hydrocarbons during serpentinization of olivine. *Geochim. Cosmochim. Ac.*
588 **65**(21), 3769-3778.

McCollom T. M. (2003) Formation of meteorite hydrocarbons from thermal decomposition of siderite ($FeCO_3$). *Geochim. Cosmochim. Ac.* **67**(2), 311-317.

McCollom T. M. and Seewald J. S. (2003) Experimental constraints on the hydrothermal reactivity of organic acids and acid anions: I. Formic acid and formate. *Geochim. Cosmochim. Ac.* **67**(19), 3625-3644.

McCollom T. M. and Seewald J. S. (2003) Experimental constraints on the hydrothermal reactivity of organic acids and acid anions: II. Acetic acid, acetate and valeric acid. *Geochim. Cosmochim. Ac.* **67**(19), 3645-3664.

McCollom T. M. and Bach W. (2009) Thermodynamic constraints on hydrogen generation during serpentinization of ultramafic rocks. *Geochim. Cosmochim. Ac.* **73**(3), 856-875.

McCollom T. M. (2013) Laboratory simulations of abiotic hydrocarbon formation in Earth's deep subsurface. In: *Carbon in Earth* (eds. R.M. Hazen, A.P. Jones, J.A. Baross), *Rev. Mineral. Geochem.* **75**, pp. 467-494. Mineralogical Society of America.

Milesi V., Prinzhofer A., Guyot F., Brunet F., Richard L., Recham N., Dairou J. and Benedetti M. (2013) Unconventional generation of hydrocarbons in petroleum basin: the role of siderite/water interface. *Mineral. Mag.* **77**, 1661-1817.

Mosmann R., Falkenhein F. U. H., Gonçalves A. and Nepomuceno Filho-F. (1987) Oil and gas potential of the Amazon Paleozoic basins. *AAPG Memoir* **27**, 207-241.

Neal C. and Stanger G. (1983) Hydrogen generation from mantle source rocks in Oman. Earth *Planet. Sci. Lett.* **66**, 315-20.

609 Perry Jr., E. C. and Ahmad S. N. (1977) Carbon isotope composition of graphite and
610 carbonate minerals from 3.8-AE metamorphosed sediments, Isukasia, Greenland. *Earth*
611 *Planet. Sc. Lett.* **36**(2), 280-284.

612 Petersen G., Viviani D., Magrini-Bair K., Kelley S., Moens L., Shepherd P. and DuBois, D.
613 (2005) Nongovernmental valorization of carbon dioxide. *Sci. total environ.* **338**(3), 159-182.

614 Pillot D., Deville E. and Prinzhofer A. (2014) Identification and quantification of carbonate
615 species using Rock-Eval pyrolysis. *Oil Gas Sci. Technol.* **69(**2), 341-349.

616 Proskurowski G., Lilley M. D., Seewald J. S., Früh-Green G. L., Olson E. J., Lupton J. E.,
617 Sylva S. P. and Kelley D. S. (2008) Abiogenic hydrocarbon production at Lost City
618 hydrothermal field. *Science* **319**(8563), 604-607.

619 Rodrigues R., Triguis J. A., Araújo C. V. and Brazil I. R. (1990) Geoquímica e faciologia
620 orgânica dos sedimentos da Bacia do Solimões. *PETROBRAS, Internal Report*, p 115.

621 Sano Y., Urabe A., Wakita H. and Wushiki H. (1993) Origin of hydrogen-nitrogen gas seeps,
622 Oman. *Appl. Geochem.*, **8**(1), 1-8.

623 Sarkar A., Seth D., Dozier A. K., Neathery J. K., Hamdeh H. H. and Davis B. H. (2007)
624 Fischer-Tropsch synthesis: Morphology, phase transformation and particle size growth of
625 nano-scale particles. *Catal. Lett.* **117**(1-2), 1-17.

626 Seewald J. S., Zolotov M. Y. and McCollom T. (2006) Experimental investigation of single
627 carbon compounds under hydrothermal conditions. *Geochim. Cosmochim. Ac.* **70**(2), 446-
628 460.

629 Steele A., McCubbin F. M., Fries M. D., Golden D. C., Ming D. W. and Benning L. G. (2012)
630 Graphite in the Martian meteorite Allan Hills 84001. *Am. Mineral.* **97**(7), 1256-1259.

631 Suda K., Ueno Y., Yoshizaki M., Nakamura H., Kurokawa K., Nishiyama E., ... and
632 Maruyama S. (2014) Origin of methane in serpentinite-hosted hydrothermal systems: The
633 CH_4–H_2–H_2O hydrogen isotope systematics of the Hakuba Happo hot spring. *Earth Planet.*
634 *Sc. Lett.* **386**, 112-125.

635 Taut T., Kleeberg R. and Bergmann J. (1998) The new Seifert Rietveld program BGMN and
636 its application to quantitative phase analysis. *Mater. Struc.* **5**, 57-66.

637 Ueno Y., Yurimoto H., Yoshioka H., Komiya T. and Maruyama S. (2002) Ion microprobe
638 analysis of graphite from ca. 3.8 Ga metasediments, Isua supracrustal belt, West Greenland:
639 Relationship between metamorphism and carbon isotopic composition. *Geochim. Cosmochim.*
640 *Ac.* **66**(7), 1257-1268.

641 van der Lee J., De Windt L., Lagneau V. and Goblet P. (2003) Module-oriented modeling of
642 reactive transport with HYTEC. *Comput. Geosci.* **29**(3), 265-275.

643 van Zuilen M. A., Lepland A., Teranes J., Finarelli J., Wahlen M. and Arrhenius G. (2003)
644 Graphite and carbonates in the 3.8 Ga old Isua Supracrustal Belt, southern West Greenland.
645 *Precambrian Res.* **126**(3-4), 331-348.

646 Voglesonger K. M., Holloway J. R., Dunn E. E., Dalla-Betta P. J. and O'Day P. A. (2001)
647 Experimental abiotic synthesis of methanol in seafloor hydrothermal systems during diking
648 events. *Chem. Geol.* **180**(1-4), 129-139.

649 Wolery T. J. (1992) EQ3/6: A software package for geochemical modeling of aqueous
650 systems: Package overview and installation guide (version 7.0). Livermore, CA: Lawrence
651 Livermore National Laboratory.

652 Zolotov M. Y. and Shock E. L. (2000) An abiotic origin for hydrocarbons in the Allan Hills
653 84001 Martian meteorite through cooling of magmatic and impact-generated gases. *Meteorit.*
654 *Planet. Sci.* **35**(3), 629-638.

Table 1. Experimental conditions (50 MPa) and gas concentrations

Experiments	Temperature (°C)	Time (hours)	CO_2	H_2	CH_4
S200-1	200	67	6.1	b.d.l.	b.d.l.
S200-2	200	1080	3.7	b.d.l.	b.d.l.
S300-1	300	3	101	12.1	b.d.l.
S300-2	300	48	213	6.9	0.07
S300-3	300	144	478	2.1	0.18
S300-4	300	168	368	0.9	0.13
S300-5	300	2880	453	1.5	0.36
Dry-Siderite	300	144	b.d.l.	b.d.l.	b.d.l.

Concentrations are in *m*molal – Error bars are of +/-20%
b.d.l – below detection limit. n.a. – not analyzed.

Added table 2

Table 2. Hydrogen mass balance calculation

Experiments	Time (h)	Measured CO_2	Expected H_2[a]	Measured H_2
S300-1	3	101	10	12.1
S300-5	2880	453	127	1.5

Concentrations are in *m*molal – Error bars are of +/-20%

[a]Expected H_2 = H_2 produced by reaction (2) calculated from measured CO_2 minus H_2 consumed by reaction (4) and (5) due to O_2 and N_2 introduced in the Au capsule (see text). Calculations are performed assuming an H_2 concentration at equilibrium with the siderite – magnetite – "graphite" mineral assemblage.

Figure captions

Figure 1. XRPD pattern and secondary electron images of the synthetic siderite used as starting material. Siderite grains exhibit well-developed faces and a homogeneous grain size distribution centered around ten to twenty of micrometers. Note the absence of iron oxide Bragg's reflections on the XRPD pattern.

Figure 2. H_2, CO_2 and CH_4 concentrations as a function of time at 300°C and 50 MPa. H_2 and CH_4 concentrations are multiplied by a factor 50 and 1000, respectively. Note that the horizontal axis (run time) has been truncated.

Figure 3. XRPD pattern and SEM images in backscattered electron mode of sample *S300-3* showing altered siderite (darker minerals) covered up with magnetite grains (lighter grains). Image (a) shows dissolution pits on the siderite surface, surrounded by smaller grains of iron oxide with typical grain sizes of ~ 100 nm. Grains of magnetite larger than 1 µm are observed, partly embedded in the siderite surface (Image b). Magnetite (dashed) is the only solid product noticeable in the XRPD pattern, along with the residual siderite (dotted).

Figure 4. TEM image of sample *S300-3* showing, attached to the carbon film, a porous C-rich phase unstable under the electron beam, interpreted as an hydrated or hydrogenated carbonaceous phase. Such phase was never observed in the starting materials.

Figure 5. High-resolution TEM images of sample *S200-1* showing details of the carbon coat which covers a magnetite crystal (a) and a siderite grain (b). The carbonaceous material shows a higher structural order when associated with magnetite.

Figure 6. High-resolution TEM images of sample *S300-3* showing iron oxide (either FeO or Fe_3O_4) closely associated to the solid carbon-rich phase at the surface of the siderite.

Figure 7. $log\, m_{H_2(aq)}$- $log\, m_{CO_2(aq)}$ diagram showing the stability domains of hematite, magnetite, wüstite and siderite as well as the CO_2 – graphite equilibrium at 50 MPa, 295°C (grey dashed lines) and 300°C (full black lines). The measured CO_2 and H_2 molalities of the 300°C experiments are also plotted. Darker symbols correspond to longer run durations. The dotted line represents the potential compositional path followed by the solution after all of the initial O_2 had reacted with H_2 and assuming stoichiometric dissolution of siderite at first.

Revised figure 1

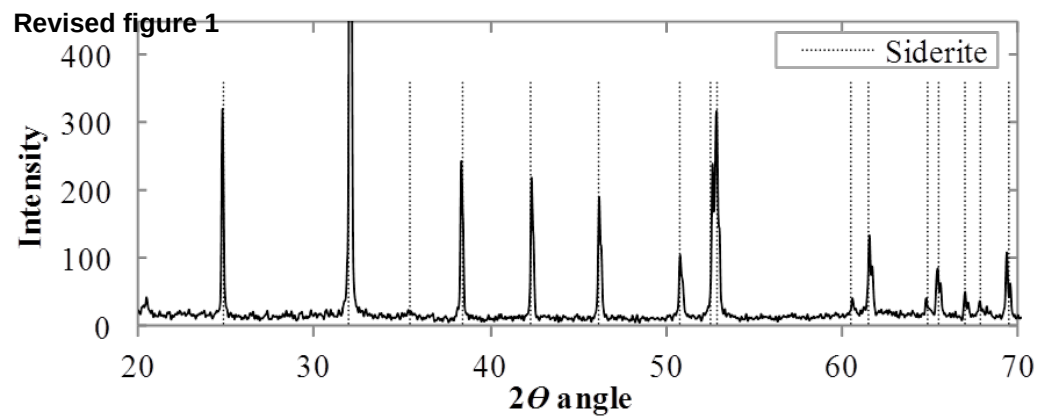

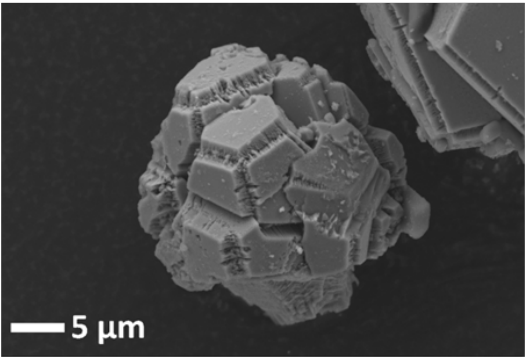

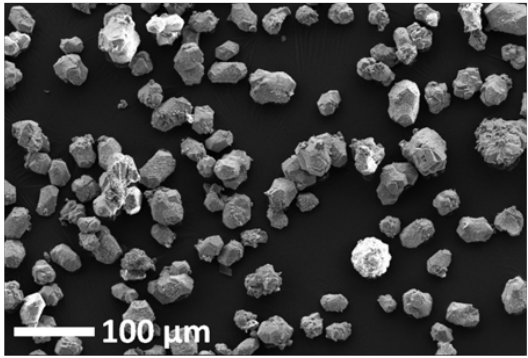

Revised figure 2

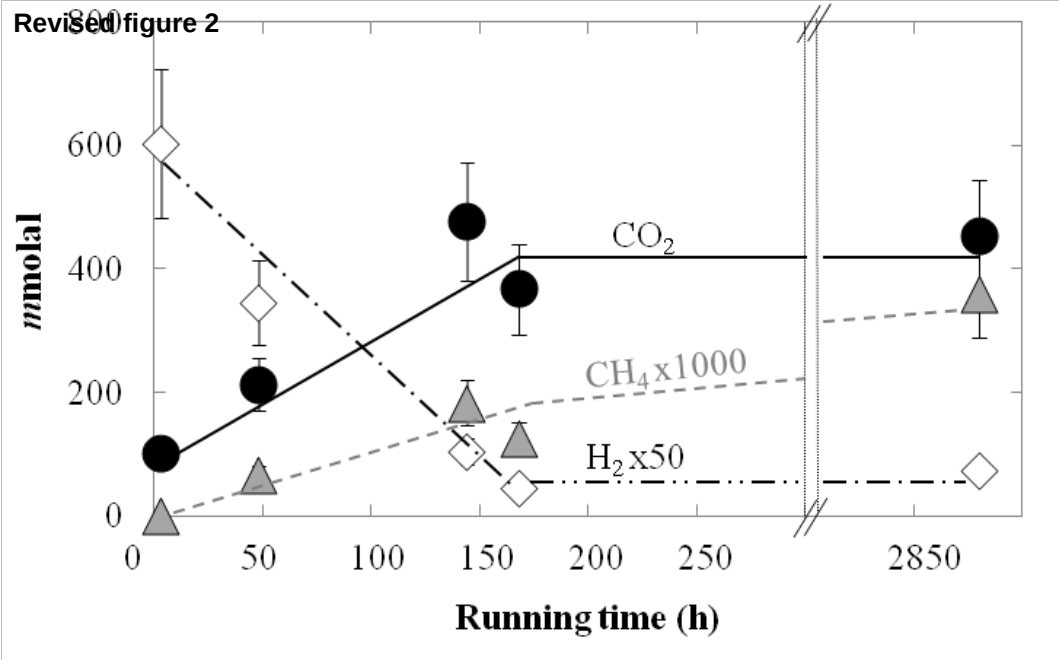

Revised figure 3

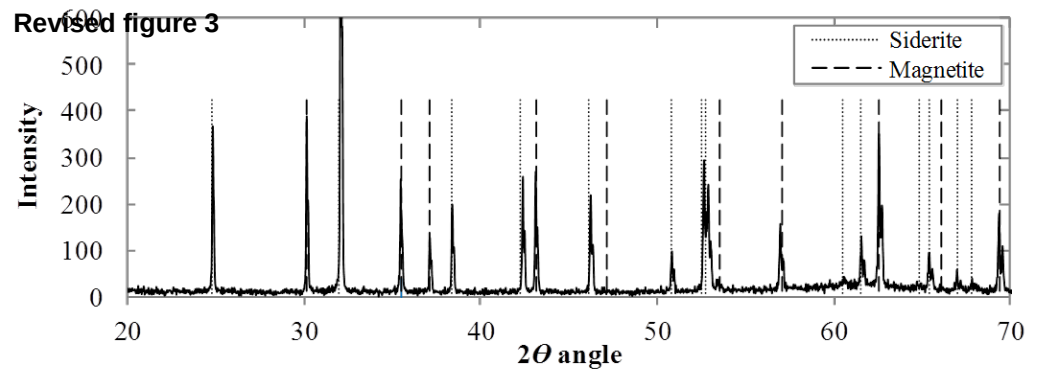

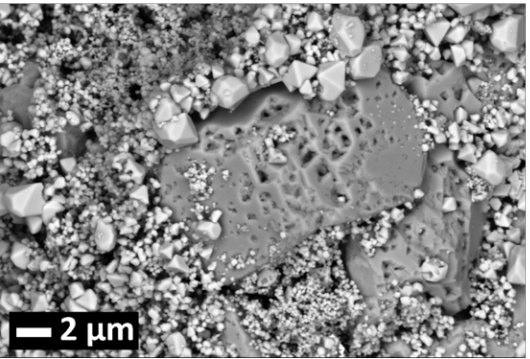

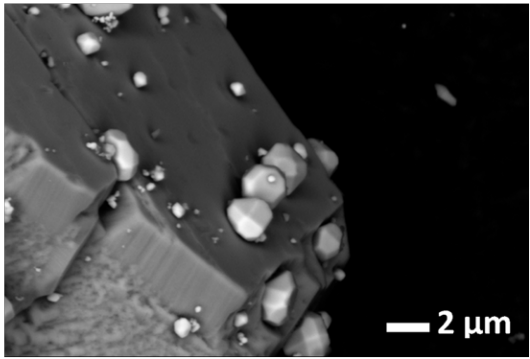

Revised figure 4

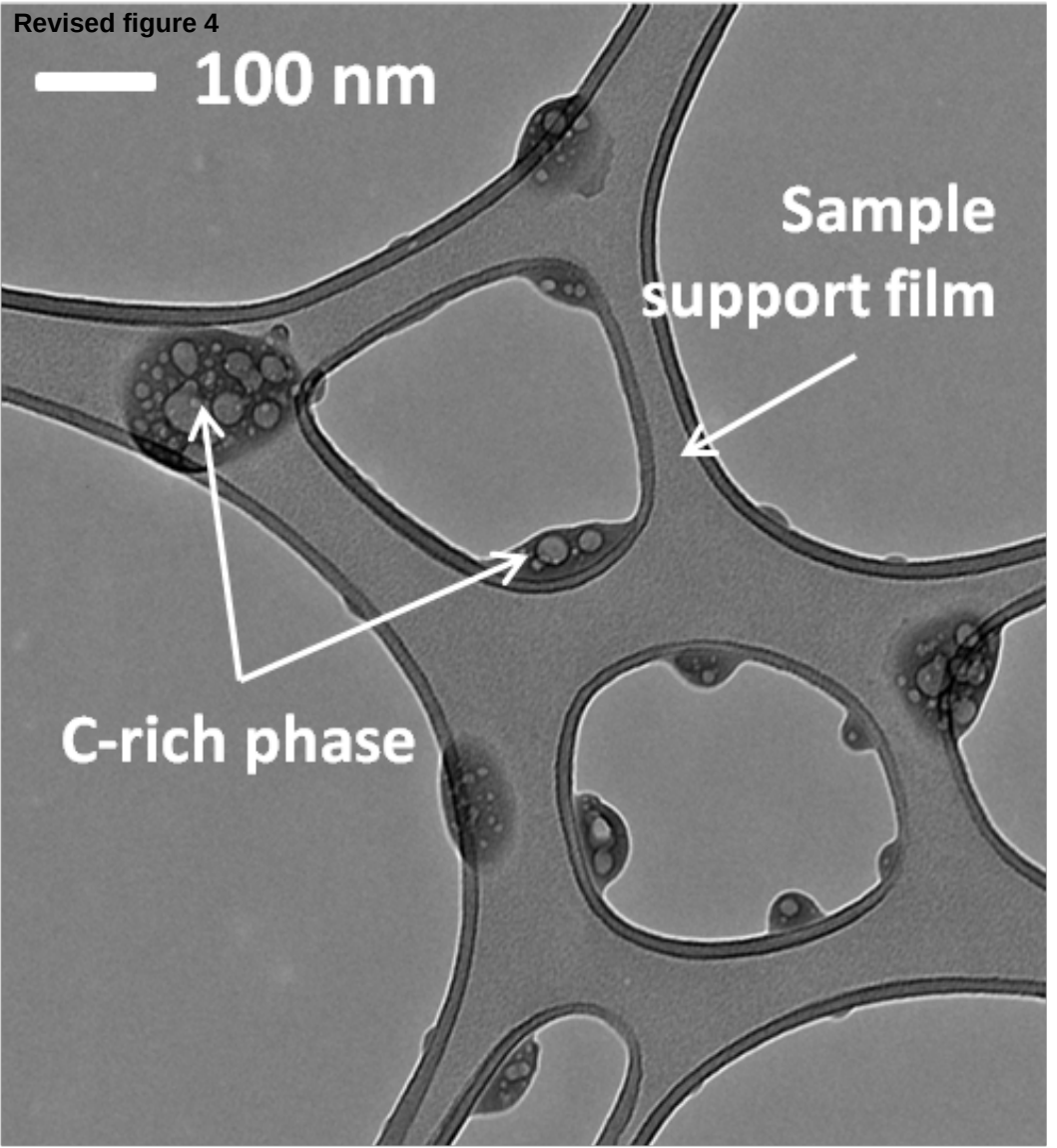

Revised figure 5

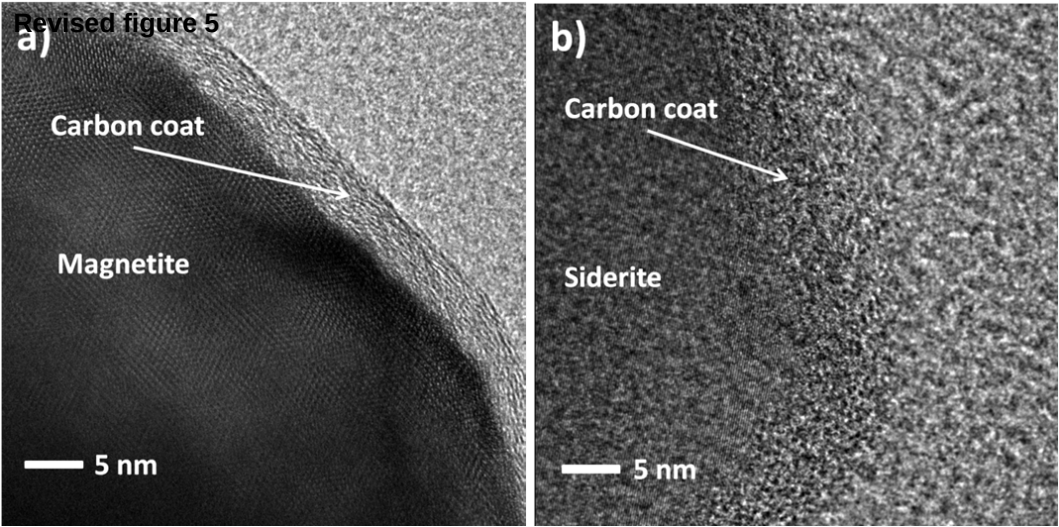

Revised figure 6

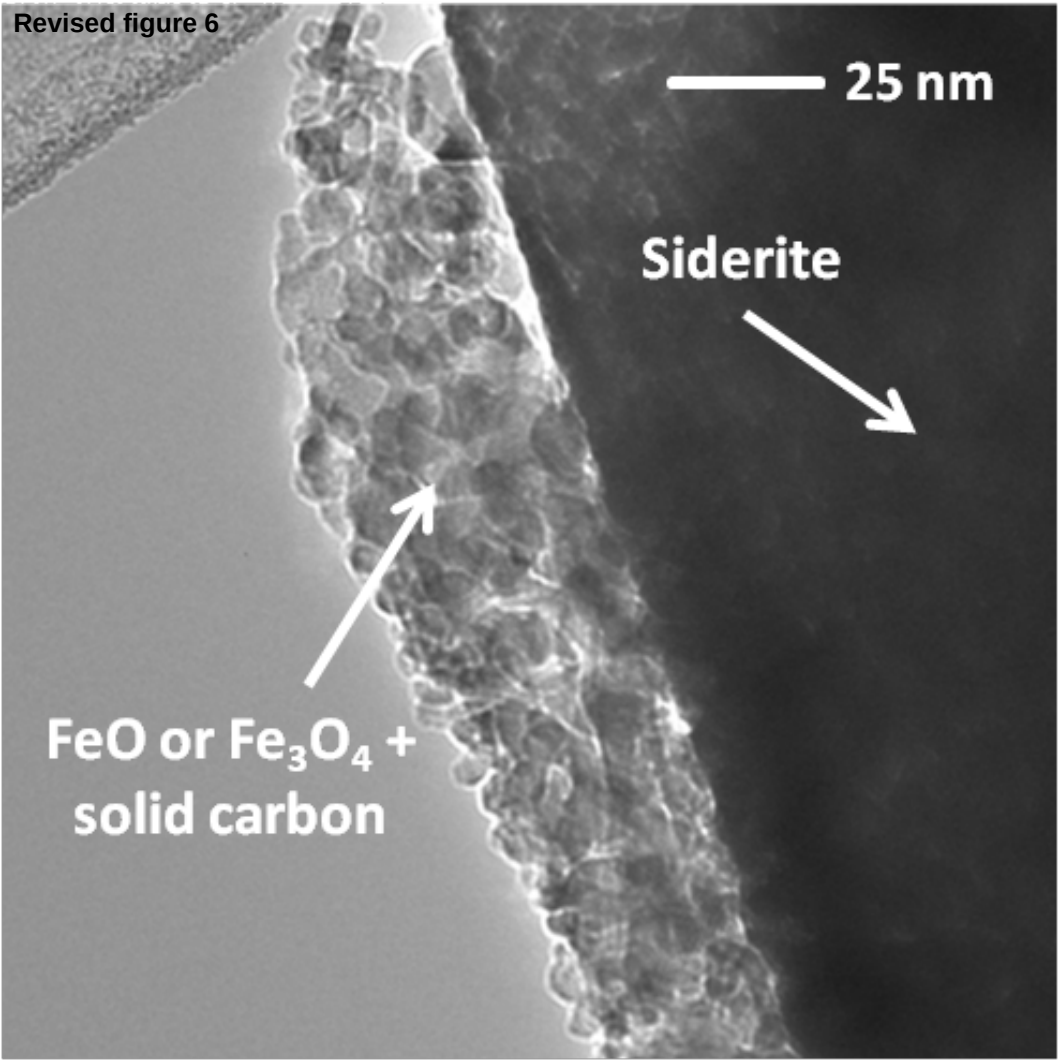

Revised figure 7